Unidirectional invisibility and $\mathcal{PT}$ symmetry with graphene

Mustafa Sarısaman*
Department of Physics, Koç University, Sarıyer 34450, Istanbul, Turkey

Murat Tas†
Institute of Nanotechnology, Gebze Technical University, Gebze 41400, Kocaeli, Turkey

(Received 29 September 2017; revised manuscript received 29 November 2017; published 9 January 2018)

We investigate the reflectionlessness and invisibility properties of the transverse electric–mode solution of a linear homogeneous optical system which comprises $\mathcal{PT}$-symmetric structures covered by graphene sheets. We derive analytic expressions, indicate the roles of each parameter governing the optical system with graphene, and prove that optimal conditions of these parameters give rise to broadband and wide-angle invisibility. The presence of graphene turns out to shift the invisible wavelength range and to reduce the required gain value considerably, based on its chemical potential and temperature. We substantiate that our results yield broadband reflectionless and invisible configurations for realistic materials of small refractive indices, usually around $\eta = 1$, and of small thicknesses with graphene sheets of rather low temperatures and chemical potentials. Finally, we demonstrate that pure $\mathcal{PT}$-symmetric graphene yields invisibility at low temperatures and chemical potentials.

DOI: 10.1103/PhysRevB.97.045409

I. INTRODUCTION

The emergence of $\mathcal{PT}$-symmetric quantum mechanics [1] stunningly elaborates the space of operators yielding real energies into the realm of non-Hermiticity. This abrupt intriguing advance has led to the commencement of studies and applications in various fields of physics [2–10], among which $\mathcal{PT}$ symmetry has found the most interest in quantum optics and related fields due to its smooth realization in experimental investigations and immediate applications [4,5,11]. A generic $\mathcal{PT}$-symmetric Hamiltonian possesses a potential whose peculiar property is $V(x) = V^{\star}(-x)$ [1,4,6]. Complex optical $\mathcal{PT}$-symmetric potentials are realized by the formal equivalence between the quantum mechanical Schrödinger equation and the optical-wave equation derived from Maxwell equations. By exploiting optical modulation of the refractive index in the complex dielectric permittivity plane and engineering both optical absorption and amplification, $\mathcal{PT}$-symmetric optical systems can lead to a series of intriguing optical phenomena and devices, such as dynamic power oscillations of light propagation, coherent perfect absorber lasers [12,13], spectral singularities [14–18], and unidirectional invisibility [4,7,8,19].

The advantage of using $\mathcal{PT}$ symmetry in optical systems is that its evolution is measurable through the quantum-optical analog. Thus, we investigated the feasibility of realizing unidirectional reflectionlessness and invisibility properties of a $\mathcal{PT}$-symmetric optical slab system by means of an optically active real material using the impressive power of a transfer matrix in the framework of the quantum scattering formalism in [19]. In the present paper we aim to increase the reflectionless and invisible wavelength interval using graphene sheets.

Graphene has well-documented physical properties and numerous applications which have attracted great interest and remained in the scientific limelight for over a decade [20]. Since the early discovery of graphene, a vast literature has been emanated and a growing number of applications has been found [21–25]. The idea that graphene may interact with electromagnetic waves in anomalous and exotic ways, providing new phenomena and applications, has given rise to the study of reflectionlessness and invisibility phenomena in $\mathcal{PT}$-symmetric optical structures with graphenes [26]. Especialy, recent works in this field performed by the method of two-dimensional cloaking and transformation optics make up the essential motivation for our work [24–26], which uses the whole competency of the transfer matrix method in the scattering formalism [28], exploiting the spectral singularities and invisibility of electromagnetic fields interacting with an optically active medium [12,13,15].

Invisibility studies in the literature bifurcate as cloaking using transformation optics and transfer matrix methods. The former exploits the beauty of transformation optics and stunning efficiency of metamaterials [29]. This approach is based on the fact that the object that is invisible is to be concealed behind an artificially manufactured material [30]. In general, graphene is considered a two-dimensional masking material. Another treatment employs the interferometric methods implemented by the transfer matrix, which has gained growing interest in recent years [16–18,27,31–39] and by which we examine the role of graphene.

In this paper we conduct a comprehensive study of unidirectional reflectionlessness and invisibility in the oblique transverse electric (TE) mode of a $\mathcal{PT}$-symmetric system with graphene to reveal the intriguing traits of the transfer matrix to be complementary to [19]. Our system is depicted in Fig. 1.

*msarisaman@ku.edu.tr
†tasm236@gmail.com

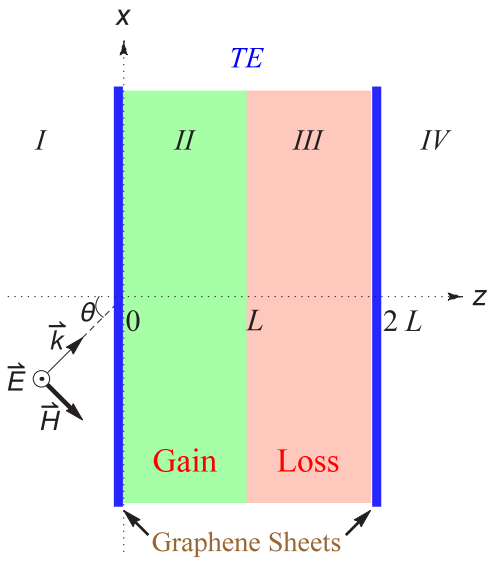

FIG. 1. Configuration of the TE mode of a slab system consisting of a pair of gain and loss layers of thickness L that are covered by graphene sheets in vacuum. I, II, III, and IV, respectively, label the regions of the space corresponding to $z<0, 0<z<L, L<z<2L$, and $z>2L$. II and III, respectively, correspond to the gain and loss layers, while I and IV represent the vacuum.

Our analysis reveals all possible configurations of solutions that support unidirectional reflectionlessness and invisibility. In particular, we obtain analytic expressions for reflectionless and invisible configurations and examine the behaviors of practically the most desirable choices of parameters corresponding to TE waves. We reveal that optimal control of parameters such as the gain coefficient, incident angle, slab thickness, temperature, and chemical potential of graphene sheets gives rise to the desired outcome of achieving a wide wavelength range of unidirectional reflectionlessness and invisibility. Thus, we provide concrete grounds that restrict the gain coefficient, wavelength, slab thickness, incidence angle, temperature, and chemical potential of graphene in certain ranges. The optimal values of these parameters should be adjusted in a given system if one desires broadband reflectionless and invisible situations. This provides valuable information on unidirectional reflectionlessness and invisibility for the possible experimental realization of a $\mathcal{PT}$-symmetric slab system with graphene. Our method and hence results are quite reliable for all realistic materials of practical concern.

II. TE-MODE SOLUTION OF A PARALLEL PAIR OF SLABS WITH GRAPHENES

Consider a $\mathcal{PT}$-symmetric planar slab system whose exterior surfaces are encompassed by graphene sheets as sketched in Fig. 1. Suppose that the entire optical system is immersed in air with refractive index $\mathfrak{n}_0=1$ and regions II and III are, respectively, filled with gain and loss materials having constant complex refractive indices $\mathfrak{n}_1$ and $\mathfrak{n}_2$. Let this system be exposed to external time harmonic electromagnetic fields, denoted, respectively, $\vec{\mathcal{E}}$ and $\vec{\mathcal{H}}$ for the electric and magnetic fields. Maxwell equations describing the interaction of the electromagnetic waves with this system have the form

$$\vec{\nabla}\cdot\vec{\mathcal{D}}=\rho(z),\quad \vec{\nabla}\cdot\vec{\mathcal{B}}=0, \tag{1}$$

$$\vec{\nabla}\times\vec{\mathcal{H}}-\partial_t\vec{\mathcal{D}}=\sigma(z)\vec{\mathcal{E}},\quad \vec{\nabla}\times\vec{\mathcal{E}}+\partial_t\vec{\mathcal{B}}=\vec{0}, \tag{2}$$

where $\vec{\mathcal{E}}$ and $\vec{\mathcal{H}}$ are connected to the $\vec{\mathcal{D}}$ and $\vec{\mathcal{B}}$ fields via the constitutive relations

$$\vec{\mathcal{D}}:=\varepsilon_0\mathfrak{z}(z)\vec{\mathcal{E}},\quad \vec{\mathcal{B}}:=\mu_0\vec{\mathcal{H}},$$

with ε_0 and μ_0, respectively, the permeability and permittivity of the vacuum. We defined

$$\mathfrak{z}(z):=\begin{cases}\mathfrak{n}_1^2 & \text{for}\quad z\in II,\\ \mathfrak{n}_2^2 & \text{for}\quad z\in III,\\ 1 & \text{otherwise},\end{cases} \tag{3}$$

such that the subindex $j=1,2$ represents the gain and loss regions of space, respectively, as depicted in Fig. 1. In the Maxwell equations, (1) and (2), $\rho(z)$ and $\sigma(z)$, respectively, denote the free charge and conductivity present on the graphene sheets and, therefore, are expressed as

$$\rho(z):=\rho_g^{(1)}\delta(z)+\rho_g^{(2)}\delta(z-2L),$$
$$\sigma(z):=\sigma_g^{(1)}\delta(z)+\sigma_g^{(2)}\delta(z-2L),$$

where $\rho_g^{(j)}$ and $\sigma_g^{(j)}$ are, respectively, the free charge and conductivity in the jth layer of graphene, with $j=1,2$. Note that $\rho(z)$ and $\sigma(z)$ are associated with each other by the continuity equation

$$\vec{\nabla}\cdot\vec{\mathcal{J}}+\partial_t\rho(z)=0 \tag{4}$$

for the electric current density $\vec{\mathcal{J}}:=\sigma(z)\vec{\mathcal{E}}$. The conductivity of graphene sheets has been determined within the random phase approximation in [40] as the sum of intraband and interband contributions, i.e., $\sigma_g=\sigma_{\rm intra}+\sigma_{\rm inter}$, where

$$\sigma_{\rm intra}:=\frac{2ie^2k_BT}{\pi\hbar^2(\omega+i\Gamma)}\ln\left[2\cosh\left(\frac{\mu}{2k_BT}\right)\right],$$
$$\sigma_{\rm inter}:=\frac{e^2}{4\hbar}\left[\frac{1}{2}+\frac{1}{\pi}\arctan\left(\frac{\hbar\omega-2\mu}{2k_BT}\right)-\frac{i}{2\pi}\ln\frac{(\hbar\omega+2\mu)^2}{(\hbar\omega-2\mu)^2+(2k_BT)^2}\right]. \tag{5}$$

Here, $-e$ is the electron charge, $\hbar$ is the reduced Planck's constant, k_B is Boltzmann's constant, Γ is the charge carrier scattering rate, T is the temperature, μ is the chemical potential, and $\hbar\omega$ is the photon energy [25]. In time harmonic forms, the $\vec{\mathcal{E}}(\vec{r},t)$ and $\vec{\mathcal{H}}(\vec{r},t)$ fields are, respectively, given by $\vec{\mathcal{E}}(\vec{r},t)=e^{-i\omega t}\vec{E}(\vec{r})$ and $\vec{\mathcal{H}}(\vec{r},t)=e^{-i\omega t}\vec{H}(\vec{r})$. Thus, Maxwell equations corresponding to TE wave solutions yield the following form of Helmholtz equations:

$$[\nabla^2+k^2\mathfrak{z}(z)]\vec{E}(\vec{r})=0,\quad \vec{H}(\vec{r})=-\frac{i}{kZ_0}\vec{\nabla}\times\vec{E}(\vec{r}), \tag{6}$$

where $\vec{r}:=(x,y,z)$, $k:=\omega/c$ is the wave number, $c:=1/\sqrt{\mu_0\varepsilon_0}$ is the speed of light in vacuum, and $Z_0:=\sqrt{\mu_0/\varepsilon_0}$ is the impedance of the vacuum. We stress that TE waves correspond to the solutions of (6) for which $\vec{\mathcal{E}}(\vec{r})$ is parallel

to the surface of the slabs. In our geometrical setup, they are aligned along the y axis. Suppose that in region I, incident wave $\vec{E}(\vec{r})$ adapts a plane wave with wave vector $\vec{k}$ in the x-z plane, specified by

$$\vec{k} = k_x\hat{e}_x + k_z\hat{e}_z, \quad k_x := k\sin\theta, \quad k_z := k\cos\theta, \tag{7}$$

where $\hat{e}_x$, $\hat{e}_y$, and $\hat{e}_z$, are, respectively, the unit vectors along the x, y, and z axes, and $\theta \in [-90^\circ, 90^\circ]$ is the incidence angle (see Fig. 1.) Then the electric field for the TE waves is given by

$$\vec{E}(\vec{r}) = \mathscr{E}(z)e^{ik_x x}\hat{e}_y, \tag{8}$$

where $\mathscr{E}$ is the solution of the Schrödinger equation

$$-\psi''(z) + v(z)\psi(z) = k^2\psi(z), \quad z \notin \{0, L, 2L\}, \tag{9}$$

for the potential $v(z) := k^2[1 + \sin^2\theta - \mathfrak{z}(z)]$. The fact that the potential $v(z)$ is constant in spaces of interest gives rise to a solution in relevant regions,

$$\psi(z) := \begin{cases} a_0\, e^{ik_z z} + b_0\, e^{-ik_z z} & \text{for} \quad z \in I, \\ a_1\, e^{i\tilde{k}_1 z} + b_1\, e^{-i\tilde{k}_1 z} & \text{for} \quad z \in II, \\ a_2\, e^{i\tilde{k}_2 z} + b_2\, e^{-i\tilde{k}_2 z} & \text{for} \quad z \in III, \\ a_3\, e^{ik_z z} + b_3\, e^{-ik_z z} & \text{for} \quad z \in IV, \end{cases} \tag{10}$$

where a_i and b_i, with $i = 0,1,2,3$, are k-dependent complex coefficients, and

$$\tilde{k}_j := k\sqrt{\mathfrak{n}_j^2 - \sin^2\theta} = k_z\tilde{\mathfrak{n}}_j, \quad \tilde{\mathfrak{n}}_j := \sec\theta\sqrt{\mathfrak{n}_j^2 - \sin^2\theta}. \tag{11}$$

In particular, $\mathscr{E}(z)$ is given by the right-hand side of (10), with generally different choices for the constants a_i and b_i. These coefficients are related to each other by means of appropriate boundary conditions, which are expressed by the fact that the tangential components of $\vec{E}$ and $\vec{H}$ are continuous across the surface, while the normal components of $\vec{H}$ have a step of unbounded surface currents across the interface of graphenes [41].

III. TRANSFER MATRIX FORMALISM

We make use of the transfer matrix, which is a useful tool for understanding the scattering properties of an optical system. For our two-layer system, the transfer matrix can be expressed as the product of the transfer matrices of the gain and loss regions. If $\mathbf{M}_1$ and $\mathbf{M}_2$ are 2×2 matrices corresponding to the slabs placed in regions of gain and loss, respectively, and $\mathbf{M} = [M_{ij}]$ is the transfer matrix of the composite system, then they all satisfy the composition property $\mathbf{M} = \mathbf{M}_2\mathbf{M}_1$, which is given by

$$\begin{bmatrix} a_3 \\ b_3 \end{bmatrix} = \mathbf{M}\begin{bmatrix} a_0 \\ b_0 \end{bmatrix}.$$

Hence, the components of the transfer matrix are determined to be

$$M_{jk} = \mathfrak{a}_j\big[U_k\big(\mathfrak{u}_j^{(2)} + j\big)e^{i\tilde{k}_2 L} + V_k\big(\mathfrak{u}_j^{(2)} - j\big)e^{-i\tilde{k}_2 L}\big], \tag{12}$$

where the subindex j, k denotes $+$, $-$, M_{++} represents the M_{11} component, and so forth. We also refer to the identifications

$$\begin{aligned} &\mathfrak{a}_\pm := \frac{e^{\mp 2ik_z L}}{8}, \quad \mathfrak{u}_\pm^{(\ell)} := \frac{1 \pm \sigma_g^{(\ell)}}{\tilde{\mathfrak{n}}_\ell}, \\ &U_\pm := (\tilde{\mathfrak{n}}_1 + \tilde{\mathfrak{n}}_2)\big(1 \pm \mathfrak{u}_\pm^{(1)}\big)e^{i\tilde{k}_1 L} + (\tilde{\mathfrak{n}}_2 - \tilde{\mathfrak{n}}_1)\big(1 \mp \mathfrak{u}_\pm^{(1)}\big)e^{-i\tilde{k}_1 L}, \\ &V_\pm := (\tilde{\mathfrak{n}}_2 - \tilde{\mathfrak{n}}_1)\big(1 \pm \mathfrak{u}_\pm^{(1)}\big)e^{i\tilde{k}_1 L} + (\tilde{\mathfrak{n}}_1 + \tilde{\mathfrak{n}}_2)\big(1 \mp \mathfrak{u}_\pm^{(1)}\big)e^{-i\tilde{k}_1 L}, \end{aligned} \tag{13}$$

with $\ell = 1,2$. It is a natural consequence of $\mathcal{PT}$ symmetry that one obtains the following relations:

$$\begin{aligned} &\mathfrak{a}_+ \overset{\mathcal{PT}}{\longleftrightarrow} \mathfrak{a}_-, \quad \tilde{\mathfrak{n}}_1 \overset{\mathcal{PT}}{\longleftrightarrow} \tilde{\mathfrak{n}}_2, \\ &\mathfrak{u}_\pm^{(1)} \overset{\mathcal{PT}}{\longleftrightarrow} \mathfrak{u}_\mp^{(2)}, \quad \sigma_g^{(1)} \overset{\mathcal{PT}}{\longleftrightarrow} -\sigma_g^{(2)}. \end{aligned} \tag{14}$$

Thus, it can be shown that components of the transfer matrix, (12), satisfy the symmetry relations in [42]

$$M_{++} \overset{\mathcal{PT}}{\longleftrightarrow} M_{--}^*, \quad M_{+-} \overset{\mathcal{PT}}{\longleftrightarrow} -M_{+-}^*, \quad M_{-+} \overset{\mathcal{PT}}{\longleftrightarrow} -M_{-+}^*.$$

We recover that current flowing on the first graphene sheet is in the opposite direction on the second graphene sheet as a consequence of $\mathcal{PT}$ symmetry. Reflection (left/right) and transmission coefficients are easily constructed to have relations of the form

$$\mathrm{R}^l = -\frac{U_+(\mathfrak{u}_-^{(2)} - 1) + V_+(\mathfrak{u}_-^{(2)} + 1)e^{-2i\tilde{k}_2 L}}{U_-(\mathfrak{u}_-^{(2)} - 1) + V_-(\mathfrak{u}_-^{(2)} + 1)e^{-2i\tilde{k}_2 L}}, \tag{15}$$

$$\mathrm{R}^r = \frac{U_-(\mathfrak{u}_+^{(2)} + 1) + V_-(\mathfrak{u}_+^{(2)} - 1)e^{-2i\tilde{k}_2 L}}{U_-(\mathfrak{u}_-^{(2)} - 1) + V_-(\mathfrak{u}_-^{(2)} + 1)e^{-2i\tilde{k}_2 L}}e^{-4ik_z L}, \tag{16}$$

$$\mathrm{T} = \mathfrak{a}_-^{-1}[U_-(\mathfrak{u}_-^{(2)} - 1)e^{i\tilde{k}_2 L} + V_-(\mathfrak{u}_-^{(2)} + 1)e^{-i\tilde{k}_2 L}]^{-1}. \tag{17}$$

Information on the (right/left) reflection and transmission coefficients provides insight into unidirectional reflectionlessness and invisibility of the optical system. If the condition $\mathrm{R}^{l/r} = 0$ together with $\mathrm{R}^{r/l} \neq 0$ is satisfied accordingly, then the optical system is called (left/right) reflectionless. In addition to this condition, one imposes the condition of $\mathrm{T} = 1$ to reveal unidirectional invisibility. We examine each case in the following sections.

IV. UNIDIRECTIONALLY REFLECTIONLESS AND INVISIBLE POTENTIALS

The (left/right) reflectionlessness is fulfilled provided that $\mathrm{R}^{l/r} = 0$ and $\mathrm{R}^{r/l} \neq 0$ hold simultaneously. Thus, one obtains the following conditions for the left/right reflectionlessness:

$$e^{-2i\tilde{k}_2 L} = \frac{U_\pm\big(1 \mp \mathfrak{u}_\mp^{(2)}\big)}{V_\pm\big(1 \pm \mathfrak{u}_\mp^{(2)}\big)}, \quad e^{-2i\tilde{k}_2 L} \neq \frac{U_\mp\big(1 \pm \mathfrak{u}_\pm^{(2)}\big)}{V_\mp\big(1 \mp \mathfrak{u}_\pm^{(2)}\big)}. \tag{18}$$

It is implied that the upper and lower relations are negations of each other if one desires to exhibit unidirectional reflectionlessness. If both relations hold simultaneously, the system is said to be bidirectionally reflectionless [43]. In addition, uni- or bidirectional invisibility is realized by exposing the condition $\mathrm{T} = 1$, which yields

$$e^{-2i\tilde{k}_2 L} = \frac{\mathfrak{a}_-^{-1}e^{-i\tilde{k}_2 L} + U_-\big(1 - \mathfrak{u}_-^{(2)}\big)}{V_-\big(1 + \mathfrak{u}_-^{(2)}\big)}. \tag{19}$$

Substitution of (19) into the first expression (18) leads to a couple of conditions belonging to the left and right invisible configurations, respectively:

$$e^{\mp 4ik_z L} = \frac{4\tilde{n}_2^2\left(1-\left[u_{\mp}^{(2)}\right]^2\right)}{U_{\pm}V_{\pm}}, \quad e^{\pm 4ik_z L} \neq \frac{4\tilde{n}_2^2\left(1-\left[u_{\pm}^{(2)}\right]^2\right)}{U_{\mp}V_{\mp}}. \tag{20}$$

Obviously these conditions point out that unidirectionally invisible configurations are obtained along the curves satisfying the foremost relations of (20) excluding the ranges of the same curves satisfying the secondary inequalities. Also, the expression for bidirectional invisibility is given in [44]. Only parameters of the optical system involving these relations take part in the invisibility configuration required. In principle, Eqs. (20) constitute complex expressions in their own rights and split into real and imaginary parts of the main expressions. Therefore, it is these real equations that determine the physical parameters of the invisible optical system. Parameters prevalent in our configuration involve the refractive indices of the gain and loss regions, thickness L of the slab, incidence angle θ, wavelength λ of the shining electromagnetic wave, temperature T, charge carrier scattering rate Γ, and chemical potential μ of graphene sheets which fulfill the graphene conductivity in (5).

V. PERTURBATIVE APPROACH TO REFLECTIONLESS AND INVISIBLE POTENTIALS: OPTIMAL CONDITIONS OF SYSTEM PARAMETERS

In this section, we derive analytic expressions that reveal general physical consequences of Eq. (20). Thus we describe (20) in terms of the quantities of direct physical relevance. We first identify the following:

$$\tilde{n} := \tilde{n}_1 = \tilde{n}_2^*, \quad \sigma_g := \sigma_g^{(1)} = -\sigma_g^{(2)*}, \quad u_{\pm} := u_{\pm}^{(1)} = u_{\mp}^{(2)*}. \tag{21}$$

We next denote the real and imaginary parts of n by η and κ so that

$$n = \eta + i\kappa, \quad \tilde{n} = \tilde{\eta} + i\tilde{\kappa}. \tag{22}$$

For most materials of practical concern, one can safely state the condition

$$|\kappa| \ll \eta - 1 < \eta,$$

such that the components $\tilde{\eta}$ and $\tilde{\kappa}$ in (22) give rise to the following, respectively, in the leading order of κ:

$$\tilde{\eta} \approx \sec\theta\sqrt{\eta^2 - \sin^2\theta}, \quad \tilde{\kappa} \approx \frac{\sec\theta\,\eta\,\kappa}{\sqrt{\eta^2-\sin^2\theta}}. \tag{23}$$

Next, we use another physically applicable parameter, the gain coefficient g, and recall its definition as given by

$$g := -2k\kappa = -\frac{4\pi\kappa}{\lambda}. \tag{24}$$

We realize that substitution of Eqs. (21)–(24) into Eqs. (18) and (20) leads to a couple of real equations connecting physical parameters of our system comprising η, g, θ, λ, L, T, Γ, and μ. The latter three parameters are just due to graphene sheets and contribute our constraint relations as long as they do not deform the physical properties of the desired graphene in use when they are slightly shifted. The parameters η and L can be chosen independently such that the corresponding g and λ can be estimated at a specific incidence angle θ. This is a reliable way to express the range of required gain values matching up to the wavelength λ. Therefore, one can adjust the range of the wavelength λ by adjusting other independent parameters. We figure out the plenary expression for the required gain values granting unidirectional reflectionlessness as [45]

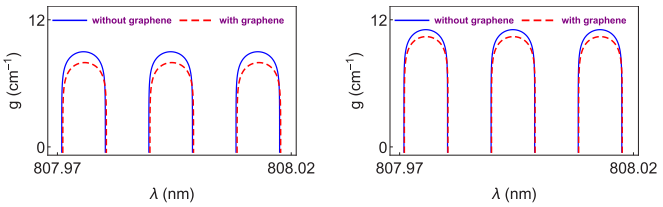

FIG. 2. The effect of graphene is illustrated via gain g versus wavelength λ plots for the values of the bilayer slab in (26) and the graphene features in (27). The left and right panels represent left and right zero-reflection conditions, respectively. We realize that graphene sheets cause gain values to alter when the wavelength pattern shifts along the horizontal axis, depending mostly on the chemical potentials and temperatures of the graphene sheets.

$$g_\ell \approx \frac{\sqrt{\eta^2-\sin^2\theta}}{\eta L}\ln\left[\frac{\mathcal{C}_\ell - \sqrt{\mathcal{C}_\ell^2 + 4\zeta_\ell^{(+)}\zeta_\ell^{(-)}}}{2\zeta_\ell^{(+)}}\right], \tag{25}$$

where $\zeta_\ell^{(\pm)}$ and $\mathcal{C}_\ell$ are denoted by

$$\zeta_\ell^{(\pm)} := (1 \pm \ell\,\mathrm{Re}[u_\ell])^2 + (\mathrm{Im}[u_\ell])^2,$$

$$\mathcal{C}_\ell := -\frac{2\tilde{\eta}}{\tilde{\kappa}}\{[1-(\mathrm{Re}[u_\ell])^2 - (\mathrm{Im}[u_\ell])^2]\sin(2k_z L\tilde{\eta}) + 2\ell\,\mathrm{Re}[u_\ell]\cos(2k_z L\tilde{\eta})\},$$

and the index $\ell = +/-$ represents the left/right reflectionless configuration. Thus, the bidirectionally reflectionless case occurs at values such that $g_+ = g_-$. To gain concrete insight into Eq. (25), we illustrate the revealing physical realizations by means of plots that reflect the basic characteristics of the gain coefficient g as a function of the wavelength λ. For this purpose, we lay out Nd:YAG crystals incorporating $\mathcal{PT}$-symmetric bilayers with the specifications

$$\eta = 1.8217, \quad L = 1\ \mathrm{cm}, \quad \theta = 30^\circ \tag{26}$$

and graphene sheets with the characterizations

$$T = 300\ \mathrm{K}, \quad \Gamma = 0.1\mathrm{meV}, \quad \mu = 0.05\ \mathrm{eV}. \tag{27}$$

Figure 2 illustrates the effect of graphene layers on a $\mathcal{PT}$-symmetric bilayer system with the specifications given in (26) and (27). We immediately observe that the gain values for unidirectional reflectionlessness are lowered and the wavelength range denoted by the size of dome shapes slightly changes in the right panel. This shows that the reflectionless wavelength width and corresponding gain values can be manipulated as desired by setting relevant temperatures and chemical potentials of graphene sheets. In these graphs, we realize that unidirectional reflectionlessness is implemented at

certain gain values in the left and right panels as pointed out in [19]. Also note that one requires higher gain values for the right reflectionlessness compared to the left. The influences of the parameters incidence angle, temperature, and chemical potential on the reflectionlessness are reported in [46].

We may use a similar approach for the perturbative expressions of the unidirectional invisibility, which give rise to transcendental equations that lead to ultimate solutions among parameters of the optical system [47]. Similar to the reflectionless case, the presence of graphene causes the invisible gain value to decrease and the wavelength interval to right-shift slightly. This means that we can obtain invisible configurations using lower gain values compared to grapheneless structures by possessing low temperatures and chemical potentials. Thus, we can observe invisibility in any wavelength range that we desire. We also observe that one requires higher gain values for the right invisibility compared to the left, and at some wavelengths the left and right invisibility gain values overlap, which produces bidirectional invisibility.

In the case of finite spread of any monochromatic light, one needs to consider a dispersion effect in the refractive index which requires κ_0 values leading to resonance gain amounts denoted by g_0 at resonance wavelength λ_0. In this case, when the wavelength is spread due to dispersion, the invisible gain amount recedes from g_0 to a higher value and wavelength slightly shifts, see [12,13] for the discussion of dispersion.

VI. EXACT ANALYSIS OF REFLECTIONLESSNESS AND INVISIBILITY

In view of the perturbative analysis of unidirectional reflectionlessness and invisibility, we are able to illustrate how the parameters of a $\mathcal{PT}$-symmetric slab system surrounded by graphene sheets react to the prescribed phenomena. Optimal values of these parameters serve for the unidirectional reflectionlessness and invisibility properties that we examine. Information on the ranges of system parameters provided by the perturbative analysis can be used to determine the extent of uni- or bidirectional reflectionlessness and invisibility. This is a natural consequence and power of the transfer matrix formalism that has to be satisfied. Therefore, we investigate graphs of the quantities $|R^l|^2$, $|R^r|^2$, and $|T-1|^2$ for various and effective system parameters as a level of reflectionlessness and invisibility. For this purpose, we directly use Eqs. (15)–(17) based on the system parameters we determined perturbatively.

Figure 3 clarifies the role of graphene in minimizing the gain value and shifting wavelength range corresponding to reflectionlessness and invisibility phenomena in the $\mathcal{PT}$-symmetric slab system. We set the slab parameters as in (26), with different choices of incidence angles, and the graphene specifications in (27). Figures in the left panels have an incidence angle $\theta = 1.305^\circ$ and wavelength $\lambda = 808$ nm with and without graphenes and represent prescribed phenomena within 2% of precision. The upper and lower left panels reveal that whereas there is no left invisibility except for two points in the absence of graphene, it occurs up to the gain value $g = 2.5\ \mathrm{cm}^{-1}$ when graphene sheets are present. Similarly, the left and right reflectionless gain values decrease in the presence of graphene (see Fig. 3). In the right panels, we employ the gain value

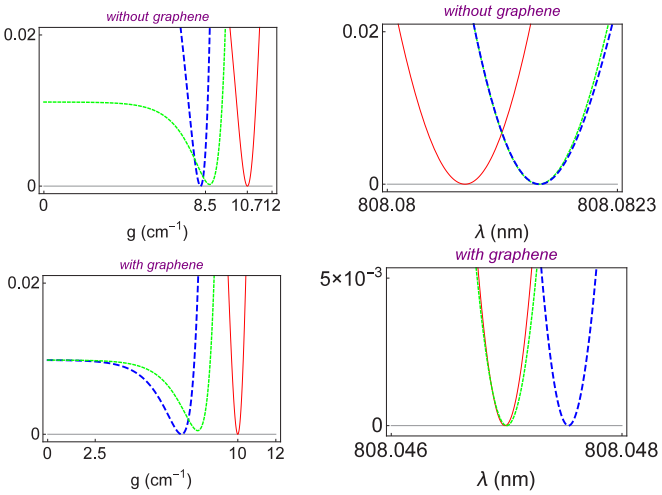

FIG. 3. Plots of $|R^l|^2$ (thick-dashed blue curve), $|R^r|^2$ (thin red curve), and $|T-1|^2$ (thin-dashed green curve) displayed on the vertical axis as a function of the amount of gain g (left) and wavelength λ (right) with and without graphenes. It is clearly shown that the required gain values for uni- or bidirectional reflectionlessness and invisibility are reduced significantly.

of $g = 8\ \mathrm{cm}^{-1}$. Right reflectionlessness and left invisibility in the absence of graphene, as shown in the upper right panel, are restricted to the wavelength interval (808.08 nm, 808.0823 nm) at incidence angle $\theta = 1.315^\circ$. The use of graphene yields right invisibility and left reflectionlessness at an incidence angle $\theta = 1.324^\circ$. Thus we conclude that graphene results in left-shifting of the wavelength range of reflectionlessness and invisibility, together with right-shifting of the angle of incidence.

The effect of other parameters on the quantities $|R^l|^2$, $|R^r|^2$, and $|T-1|^2$ is reported in [48]. We observe that graphene results in left-shifting of the wavelength range of reflectionlessness and invisibility, together with right-shifting of the angle of incidence. Also, it is obvious that all unidirectionally reflectionless and invisible patterns take place at low chemical potentials, typically less than $|\mu| = 1$ eV within 1% precision. Reducing the chemical potential to very close to 0 gives rise to quite reliable patterns. As to the temperature of graphene, we reveal that almost all accessible temperature values produce left and right reflectionless and invisible patterns, but the lowest possible temperatures engender the most precise configurations. The angle range of unidirectional reflectionlessness and invisibility decreases, and the frequency of invisibility is lower compared to that of reflectionlessness. The best angle choices are those which are very close to 0.

In Fig. 4, we reveal the consistency of our findings regarding the values parameters of the system must satisfy in order to generate the desired broadband reflectionless and invisible configurations. For this purpose, we choose aluminum as the slab material, whose refractive index is $\eta_{Al} = 1.0972$ [49], and use two thickness values, $L = 50$ nm (left panel) and $L = 10$ nm (right panel) to show the effect of the thickness. We employ very low temperature and chemical potential values for graphene as we have explored in Figs. 9 and 10 in [50], $T = 5$ K and $\mu = 5 \times 10^{-7}$ eV. We realize that distinct phenomena are

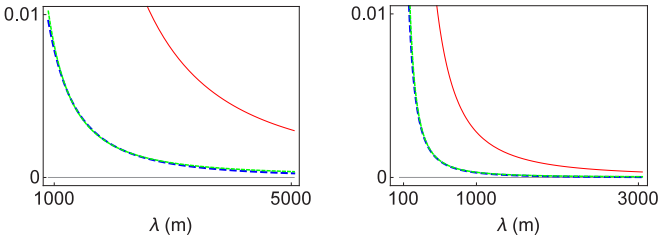

FIG. 4. Plots of $|R^l|^2$ (thick-dashed blue curve), $|R^r|^2$ (thin red curve), and $|T-1|^2$ (thin-dashed green curve) as a function of the wavelength λ for slab thicknesses $L = 50$ nm (left) and $L = 10$ nm (right) using aluminum as the slab material. As the incidence angle changes, one observes broadband unidirectional reflectionless and invisible configurations.

observed within 1% precision, depending on the incidence angle. The left panel shows left invisibility in a broad wavelength range (900 nm, 3300 nm) and right reflectionlessness in the wavelength range $\lambda \geqslant 2550$ nm at an angle of incidence $\theta = 62.6^\circ$. Although we choose a specific incidence angle yielding corresponding phenomena, there is about a 1° angle of extensibility for the same phenomena. As for the right panel, with slab thickness $L = 10$ nm, the phenomenon under study is observed in a manner where the corresponding wavelength range widens and covers a broadband even less than the visible spectrum. When the incidence angle is set to $\theta = 62.8^\circ$, we obtain left invisibility in the wavelength interval $\lambda \geqslant 165$ nm and right reflectionlessness in the range $\lambda \geqslant 500$ nm. The dependence of broadband reflectionless and invisible configurations on the incidence angle is reported in [51]. We see that the best invisible and reflectionless configurations are observed once the slab thickness is lowered to nanometer sizes. As is understood from Fig. 4, the slab thickness is rather inclusive and crucial for realization of the invisibility phenomenon. In fact, when all other parameters are fixed, the slab thickness shows a behavior of dome patterns that allows invisible gain values in periodically changing intervals of thickness sizes as in Fig. 2. This shows that not all thickness values are suitable for obtaining invisibility once other parameters are fixed. Thickness tolerance occurs within 1 nm, and when taking thicknesses around the boundaries of the dome the lowest gain value is obtained. As the size of the slab is decreased, the required gain amount increases considerably. In this case one needs a very sensitive slab size corresponding to the dome boundaries, which results in a low gain and the widest spectral range for invisibility.

VII. PURE $\mathcal{PT}$-SYMMETRIC GRAPHENE INVISIBILITY

Consider the special case where our $\mathcal{PT}$-symmetric slab is removed by setting the slab thickness L to 0, i.e., $L = 0$. This case in fact contains a slab material content with zero thickness between graphene layers, namely, there is an implicit interface ingredient between graphene sheets. One requires also $\mathfrak{n}_1 = \mathfrak{n}_2 = 0$ to suppress this interface substance. But as we see below, even this case does not affect the graphene invisibility feature since the reflection and transmission amplitudes do not depend upon the refractive indices $\mathfrak{n}_1$ and $\mathfrak{n}_2$. Setting $L = 0$

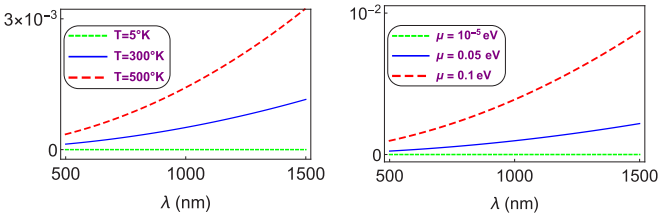

FIG. 5. Invisibility of pure $\mathcal{PT}$-symmetric graphene sheets. The vertical axis represents $|R^l|^2 = |R^r|^2 = |T-1|^2$, and the horizontal axis the wavelength λ, for different temperatures T (left) and different chemical potentials μ (right). Perfect broadband invisibility is observed at very low temperatures and chemical potentials.

simply yields that

$$R^l = R^r = \frac{\mathrm{Im}[\sigma_g]}{\mathrm{Im}[\sigma_g]+i}, \quad T = \frac{i}{\mathrm{Im}[\sigma_g]+i}.$$

Hence, note that $R^l = R^r = 1 - T$ and $|R^l|^2 = |R^r|^2 = |T-1|^2$. Therefore, at all temperatures and chemical potentials one observes bidirectional invisibility for pure $\mathcal{PT}$-symmetric graphene sheets. The measure of invisibility is improved by reducing the temperature T and chemical potential μ as sketched in Fig. 5. In the left panel we take $\mu = 10^{-5}$eV for the chemical potential, and in the right panel, $T = 5^\circ K$ for the temperature. We observe that even at high temperatures and chemical potentials, the invisibility level is less than 1%. Perfect broadband invisibility is realized at near-absolute-zero temperature and zero chemical potential.

VIII. CONCLUDING REMARKS

This paper aims to engender the role played by graphene sheets in unidirectional reflectionlessness and invisibility and their optical realizations. We determine that graphene sheets covering a $\mathcal{PT}$-symmetric slab system respect the trait of $\mathcal{PT}$ symmetry. We show that overall $\mathcal{PT}$-symmetry conditions cause surface currents flowing in opposite directions. $\mathcal{PT}$ symmetry guarantees the existence of reflectionlessness and invisibility, due to its ability to control the system parameters, as distinct from non-$\mathcal{PT}$-symmetric structures, once the appropriate parameters are inserted into the optical system, whereas just one gain or loss region does not yield this phenomenon.

We employ the elegant transfer matrix method to extract information on the reflectionless and invisible configurations, which emphasizes the power of boundary conditions arising from solutions coming directly from Maxwell equations. The availability of graphene appears in boundary conditions in the form of the complex function $\mathfrak{u}_\pm^{(j)}$ [see Eq. (13)]. In our analysis, we are able to derive the exact uni- or bidirectional expressions as seen in Eqs. (18)–(20) relating parameters of the $\mathcal{PT}$-symmetric optical system with graphene. We utilize the perturbative approach as a tool to demonstrate the optimal conditions arising from the system parameters.

In view of our findings, one can shape the reflectionless and invisible patterns provided that the parameters specifying the graphene and bilayer slab system are well adjusted. Our primary purpose in placing graphene was to widen the reflectionless and invisible wavelength range together with the wide

incidence angle interval $\Delta\theta$. We explore the achievement of this at small slab thicknesses, usually scaled down to nanometer levels; low temperatures, with the best results obtained near the value of absolute zero; and quite low chemical potentials, typically around 0. Depending upon the incidence angle, left or right reflectionless and invisible configurations can be arranged. Furthermore, it is observed that graphene causes the necessary gain value to decrease and the wavelength interval defined for the desired phenomena to shift. Another natural consequence is that the incidence angles yielding reflectionless and invisible patterns are dislocated in compatibility with the chemical potentials and temperatures of the graphene sheets.

We find out that broadband invisibility is realized at very small slab thickness values, less than the wavelength λ, which is typically on the nanometer scale, together with the corresponding material type in a slab with a low refractive index, characteristically around $\eta = 1$ and $\eta < 1.5$, as shown in Fig. 4. This is because the effect of graphene is increased when the amount of slab is decreased. In light of this consideration, we are able to show that a pure $\mathcal{PT}$-symmetric graphene structure builds perfect invisibility at tiny temperatures and chemical potentials near 0. Finally, since broadband reflectionless and invisible configurations are very sensitive to material type, which is denoted by the refractive index, an extensive analysis of different material types could be considered through our method, which would feature the use of metamaterials in $\mathcal{PT}$-symmetric graphene structures.

[1] C. M. Bender and S. Boettcher, Phys. Rev. Lett. **80**, 5243 (1998).

[2] A. Mostafazadeh, Int. J. Geom. Meth. Mod. Phys. **7**, 1191 (2010); C. M. Bender, D. C. Brody, and H. F. Jones, Am. J. Phys. **71**, 1095 (2003).

[3] B. Bagchi and C. Quesne, Phys. Lett. A **273**, 285 (2000).

[4] A. Guo, G. J. Salamo, D. Duchesne, R. Morandotti, M. Volatier-Ravat, V. Aimez, G. A. Siviloglou, and D. N. Christodoulides, Phys. Rev. Lett. **103**, 093902 (2009).

[5] B. Christian, E. Rüter, K. G. Makris, R. El-Ganainy, D. N. Christodoulides, M. Segev, and D. Kip, Nat. Phys. **6**, 192 (2010); L. Feng, M. Ayache, J. Huang, Y. Xu, M. Lu, Y. Chen, Y. Fainman, and A. Scherer, Science **333**, 729 (2011).

[6] L. Chen, R. Li, N. Yang, D. Chen, and L. Li, Proc. Rom. Acad. A **13**, 46 (2012); R. Li, P. Li, and L. Li, Proc. Roman. Acad. A **14**, 121 (2013).

[7] L. Feng, Y. L. Xu, W. S. Fegadolli, M. H. Lu, J. E. Oliveira, V. R. Almeida, Y. F. Chen, and A. Scherer, Nat. Mater. **12**, 108 (2013).

[8] Y. Shen, X. H. Deng, and L. Chen, Opt. Express **22**, 19440 (2014).

[9] A. A. Zyablovsky, A. P. Vinogradov, A. A. Pukhov, A. V. Dorofeenko, and A. A. Lisyansky, Phys. Usp. **57**, 1063 (2014).

[10] W.-X. Yang, A.-X. Chen, X.-T. Xie, and L. Ni, Phys. Rev. A **96**, 013802 (2017); J. P. Deka and A. K. Sarma, arXiv:1706.02512; F. Loran and A. Mostafazadeh, arXiv:1705.00500.

[11] Y. Huang, Y. Shen, C. Min, S. Fan, and G. Veronis, Nanophotonics **6**, 977 (2017); X. Wu, C. Jin, and C. Fu, Opt. Commun. **402**, 507 (2017); P. A. Kalozoumis, C. V. Morfonios, G. Kodaxis, F. K. Diakonos, and P. Schmelcher, Appl. Phys. Lett. **110**, 121106 (2017).

[12] A. Mostafazadeh and M. Sarisaman, Phys. Lett. A **375**, 3387 (2011); Proc. R. Soc. Lond. Ser. A Math. Phys. Eng. Sci. **468**, 3224 (2012); Phys. Rev. A **87**, 063834 (2013); **88**, 033810 (2013); A. Mostafazadeh and M. Sarısaman, *ibid.* **91**, 043804 (2015).

[13] A. Mostafazadeh and M. Sarısaman, Ann. Phys. (NY) **375**, 265 (2016).

[14] M. A. Naimark, Trudy Moscov. Mat. Obsc. **3**, 181 (1954) [in Russian] [English translation: Am. Math. Soc. Transl. (2) **16**, 103 (1960)]. For a list of mathematical literature on spectral singularities see the review article by G. Sh. Guseinov, Pramana J. Phys. **73**, 587 (2009) and Ref. [15].

[15] A. Mostafazadeh, Physics of spectral singularities, in *Geometric Methods in Physics*, edited by P. Kielanowski, P. Bieliavsky, A. Odzijewicz, M. Schlichenmaier, and T. Voronov, Trends in Mathematics (Birkhäuser, Cham, Switzerland, 2015), pp. 145–165.

[16] A. Mostafazadeh, Phys. Rev. A **87**, 012103 (2013).

[17] S. Longhi, Phys. Rev. A **82**, 032111 (2010).

[18] S. Longhi, J. Phys. A **44**, 485302 (2011).

[19] M. Sarısaman, Phys. Rev. A **95**, 013806 (2017).

[20] A. K. Geim and K. S. Novoselov, Nat. Mater. **6**, 183 (2007); A. K. Geim, Science **324**, 1530 (2009); A. H. C. Neto, F. Guinea, N. M. R. Peres, K. S. Novoselov, and A. K. Geim, Rev. Mod. Phys. **81**, 109 (2009); O. V. Yazyev, Rep. Progr. Phys. **73**, 056501 (2010).

[21] F. Schedin, A. K. Geim, S. V. Morozov, E. W. Hill, P. Blake, M. I. Katsnelson, and K. S. Novoselov, Nat. Mater. **6**, 652 (2007); R. Stine, J. T. Robinson, P. E. Sheehan, and Cy R. Tamanaha, Adv. Mater. **22**, 5297 (2010); G. Lu, L. E. Ocola, and J. Chen, Appl. Phys. Lett. **94**, 083111 (2009); J. T. Robinson, F. K. Perkins, E. S. Snow, Z. Wei, and P. E. Sheehan, Nano Lett. **8**, 3137 (2008); Y. Shao, J. Wang, H. Wu, J. Liu, I. A. Aksay, and Y. Lin, Electroanalysis **22**, 1027 (2010); Q. He, S. Wu, Z. Yin, and H. Zhang, Chem. Sci. **3**, 1764 (2012); S. Wu, Q. He, C. Tan, Y. Wang, and H. Zhang, Small **9**, 1160 (2013).

[22] J. Duffy, J. Lawlor, C. Lewenkopf, and M. S. Ferreira, Phys. Rev. B **94**, 045417 (2016).

[23] S. Chen, Z. Han, M. M. Elahi, K. M. M. Habib, L. Wang, B. Wen, Y. Gao, T. Taniguchi, K. Watanabe, J. Hone, A. W. Ghosh, and C. R. Dean, Science **353**, 1522 (2016).

[24] P.-Y. Chen and A. Alu, ACS Nano **5**, 5855 (2011); M. Danaeifar and N. Granpayeh, J. Opt. Soc. Am. B **33**, 1764 (2016).

[25] M. Naserpour, C. J. Zapata-Rodríguez, S. M. Vuković, and M. R. Belić, arXiv:1701.02487.

[26] P.-Y. Chen, J. Soric, and A. Alú, Adv. Mater. **24**, OP281 (2012).

[27] Z. Lin, H. Ramezani, T. Eichelkraut, T. Kottos, H. Cao, and D. N. Christodoulides, Phys. Rev. Lett. **106**, 213901 (2011).

[28] A. Mostafazadeh, Phys. Rev. Lett. **102**, 220402 (2009).

[29] J. B. Pendry, D. Schurig, and D. R. Smith, Science **312**, 1780 (2006); U. Leonhardt, *ibid.* **312**, 1777 (2006).

[30] W. Cai and V. Shalaev, *Optical Metamaterials: Fundamentals and Applications* (Springer, New York, 2010); N. Engheta and R. W. Ziolkowski, *Metamaterials, Physics and Engineering Ex-*

plorations (IEEE-Wiley, New York, 2006); G. V. Eleftheriades and K. G. Balmain, *Negative-Refraction Metamaterials* (IEEE, New York, 2005).
[31] A. Mostafazadeh, Phys. Rev. A **92**, 023831 (2015).
[32] A. Mostafazadeh, Phys. Rev. A **91**, 063812 (2015).
[33] S. Longhi, J. Phys. A **47**, 485302 (2014).
[34] A. Mostafazadeh, Phys. Rev. A **90**, 023833 (2014); **90**, 055803 (2014).
[35] L. L. Sanchez-Soto and J. J. Monzon, Symmetry **6**(2), 396 (2014).
[36] B. Midya, Phys. Rev. A **89**, 032116 (2014).
[37] A. Mostafazadeh, J. Phys. A **47**, 125301 (2014).
[38] A. Mostafazadeh, Phys. Rev. A **89**, 012709 (2014).
[39] S. Longhi and G. D. Valle, Ann. Phys. **334**, 35 (2013).
[40] B. Wunsch, T. Stauber, F. Sols, and F. Guinea, New J. Phys. **8**, 318 (2006); E. H. Hwang and S. D. Sarma, Phys. Rev. B **75**, 205418 (2007); L. A. Falkovsky, Phys. Usp. **51**, 887 (2008).
[41] See Supplemental Material at http://link.aps.org/supplemental/10.1103/PhysRevB.97.045409 for secured boundary conditions.
[42] A. Mostafazadeh, J. Phys. A **47**, 505303 (2014).
[43] See Supplemental Material at http://link.aps.org/supplemental/10.1103/PhysRevB.97.045409 for the expression of bidirectional reflectionlessness.
[44] See Supplemental Material at http://link.aps.org/supplemental/10.1103/PhysRevB.97.045409 for the expression of bidirectional invisibility.
[45] See Supplemental Material at http://link.aps.org/supplemental/10.1103/PhysRevB.97.045409 for the details.
[46] See Supplemental Material at http://link.aps.org/supplemental/10.1103/PhysRevB.97.045409 for the influences of the parameters incidence angle, temperature, and chemical potential on the reflectionlessness.
[47] See Supplemental Material at http://link.aps.org/supplemental/10.1103/PhysRevB.97.045409 for the details and related expressions.
[48] See Supplemental Material at http://link.aps.org/supplemental/10.1103/PhysRevB.97.045409 for the effect of other parameters on the quantities $|R^l|^2$, $|R^r|^2$, and $|T-1|^2$].
[49] A. D. Rakić, A. B. Djurišic, J. M. Elazar, and M. L. Majewski, Appl. Opt. **37**, 5271 (1998).
[50] See Supplemental Material at http://link.aps.org/supplemental/10.1103/PhysRevB.97.045409 for the details.
[51] See Supplemental Material at http://link.aps.org/supplemental/10.1103/PhysRevB.97.045409 for the dependence of broadband reflectionless and invisible configurations on the incidence angle.